arXiv:1202.4265v2 [physics.comp-ph] 21 Feb 2012

Multi-moment advection scheme in three dimension for Vlasov simulations of magnetized plasma

Takashi Minoshima[a,*], Yosuke Matsumoto[b], Takanobu Amano[c]

[a] *Institute for Research on Earth Evolution, Japan Agency for Marine-Earth Science and Technology, 3173-25, Syowa-machi, Kanazawaku, Yokohama 236-0001, Japan*
[b] *Department of Physics, Chiba University, 1-33, Yayoi-cho, Inage-ku, Chiba, 263-8522, Japan*
[c] *Department of Physics, Nagoya University, Furo-cho, Chikusa-ku, Nagoya 464-8602, Japan*

Abstract

We present an extension of the multi-moment advection scheme (Minoshima et al., 2011, J. Comput. Phys.) to the three-dimensional case, for full electromagnetic Vlasov simulations of magnetized plasma. The scheme treats not only point values of a profile but also its zeroth to second order piecewise moments as dependent variables, and advances them on the basis of their governing equations. Similar to the two-dimensional scheme, the three-dimensional scheme can accurately solve the solid body rotation problem of a gaussian profile with little numerical dispersion or diffusion. This is a very important property for Vlasov simulations of magnetized plasma. We apply the scheme to electromagnetic Vlasov simulations. Propagation of linear waves and nonlinear evolution of the electron temperature anisotropy instability are successfully simulated with a good accuracy of the energy conservation.

Keywords: Advection equation, Conservative form, Multi-moment, Vlasov simulations, Magnetized plasma

1. Introduction

The kinematics of collisionless plasma has been studied in a wide variety of fields, such as in laboratory plasma physics, space physics, and

*Corresponding author. Tel.: +81-45-778-5887; Fax: +81-45-778-5490
Email address: minoshim@jamstec.go.jp (Takashi Minoshima)

astrophysics. Evolution of collisionless plasma and self-consistent electromagnetic fields is fully described by the Vlasov-Maxwell (or Vlasov-Poisson) equations. Thanks to recent development in computational technology, self-consistent numerical simulations of collisionless plasma have been successfully performed from the first-principle Vlasov-Maxwell system of equations.

One of the numerical simulation methods for collisionless plasma is so-called Vlasov simulation, in which the Vlasov equation is directly discretized on grid points in phase space. Compared to the most popular Particle-In-Cell (PIC) method (Birdsall and Langdon, 1991), the Vlasov simulation is free from the statistical noise inherent to the PIC method. This advantage can allow us to study in detail such as wave-particle interaction, particle acceleration, and thermal transport processes, in which a high energy tail in the velocity distribution function plays an important role. On the other hand, the Vlasov simulation requires a highly accurate scheme for the advection equation in multidimensions, to preserve characteristics of the Vlasov equation (i.e., the Liouville theorem) as much as possible. It also requires larger computational cost than the PIC method.

A number of advection schemes have been proposed for the application to the Vlasov simulation thus far (e.g., Cheng and Knorr, 1976; Nakamura and Yabe, 1999; Filbet et al., 2001; Mangeney et al., 2002; Crouseilles et al., 2009). Although the schemes have been succeeded especially in applying to the electrostatic Vlasov-Poisson simulation, the application to the electromagnetic Vlasov simulation of magnetized plasma is still limited, mainly owing to the difficulty in solving the gyro motion around the magnetic field line (solid body rotation in velocity space).

Minoshima et al. (2011) have proposed a new numerical scheme for the advection equation, specifically designed to solve the Vlasov equation in magnetized plasma. The scheme treats not only point values of a profile but also its zeroth to second order piecewise moments as dependent variables, and advances them on the basis of their governing equations, for better conservation of the information entropy and reducing numerical diffusion. In the paper, we have presented one- and two-dimensional schemes, and have shown their quite high capabilities. Especially, the two-dimensional scheme can accurately solve the solid body rotation problem of a gaussian profile with little numerical dispersion or diffusion. These schemes have been successfully applied to electrostatic and electromagnetic Vlasov simulations.

For the application of the electromagnetic Vlasov simulation to a wide variety of magnetized plasma phenomena, however, it is necessary to de-

velop a three-dimensional scheme to treat the full three-dimensional velocity space. In this paper, we present an extension of our previous schemes to the three-dimensional case. Similar to the one- and two-dimensional schemes, the three-dimensional scheme treats the zeroth to second order piecewise moments as well as point values of a profile as dependent variables. Details of the scheme are described in Section 2. Benchmark tests of the scheme are presented in Section 3. The application of the scheme to electromagnetic Vlasov simulations is presented in Section 4. Finally, we summarize the paper in Section 5.

2. Three-dimensional multi-moment advection scheme (MMA3D)

We consider the time evolution of a three-dimensional profile $f(x, y, z, t)$ and its zeroth to second order moments in the x, y, and z directions defined as

$$M^0 = \iiint f dV \left(= M_x^0 = M_y^0 = M_z^0\right), \tag{1}$$

$$M_x^m = \frac{1}{m!} \iiint x^m f dV, \quad (m = 1, 2), \tag{2}$$

$$M_y^m = \frac{1}{m!} \iiint y^m f dV, \quad (m = 1, 2), \tag{3}$$

$$M_z^m = \frac{1}{m!} \iiint z^m f dV, \quad (m = 1, 2), \tag{4}$$

where $dV = dxdydz$. The conservative advection equation of f and governing equations of the moments are written as

$$\frac{\partial f}{\partial t} + u\frac{\partial f}{\partial x} + v\frac{\partial f}{\partial y} + w\frac{\partial f}{\partial z} = -\left(\frac{\partial u}{\partial x} + \frac{\partial v}{\partial y} + \frac{\partial w}{\partial z}\right) f, \tag{5}$$

$$\frac{\partial M^0}{\partial t} + \int dx \frac{\partial}{\partial x}\left(\iint u f dydz\right) + \int dy \frac{\partial}{\partial y}\left(\iint v f dzdx\right) + \int dz \frac{\partial}{\partial z}\left(\iint w f dxdy\right) = 0, \tag{6}$$

$$\frac{\partial M_x^m}{\partial t} + \int dx \frac{\partial}{\partial x}\left(\frac{x^m}{m!} \iint u f dydz\right) + \int dy \frac{\partial}{\partial y}\left(\frac{1}{m!} \iint v x^m f dzdx\right) + \int dz \frac{\partial}{\partial z}\left(\frac{1}{m!} \iint w x^m f dxdy\right)$$
$$= \frac{1}{(m-1)!} \iiint u x^{m-1} f dV, \quad (m = 1, 2), \tag{7}$$

$$\frac{\partial M_y^m}{\partial t} + \int dx \frac{\partial}{\partial x}\left(\frac{1}{m!} \iint u y^m f dydz\right) + \int dy \frac{\partial}{\partial y}\left(\frac{y^m}{m!} \iint v f dzdx\right) + \int dz \frac{\partial}{\partial z}\left(\frac{1}{m!} \iint w y^m f dxdy\right)$$
$$= \frac{1}{(m-1)!} \iiint v y^{m-1} f dV, \quad (m = 1, 2), \tag{8}$$

$$\frac{\partial M_z^m}{\partial t} + \int dx \frac{\partial}{\partial x}\left(\frac{1}{m!} \iint u z^m f dydz\right) + \int dy \frac{\partial}{\partial y}\left(\frac{1}{m!} \iint v z^m f dzdx\right) + \int dz \frac{\partial}{\partial z}\left(\frac{z^m}{m!} \iint w f dxdy\right)$$
$$= \frac{1}{(m-1)!} \iiint w z^{m-1} f dV, \quad (m = 1, 2), \tag{9}$$

where u, v, and w are the velocity component in the x, y, and z directions. Here, the conservative advection equation of f is cast into the advective form. Eqs. (6)-(9) are obtained by multiplying Eq. (5) by $x^m/m!$, $y^m/m!$, or $z^m/m!$, and then integrating over space. Hereafter, we assume $\partial u/\partial x = \partial v/\partial y = \partial w/\partial z = 0$, because we are concerned with the Vlasov equation. We use vector forms $\boldsymbol{M}^m = \left(M_x^m, M_y^m, M_z^m\right)$, $\boldsymbol{x} = (x, y, z)$, and $\boldsymbol{u} = (u, v, w)$.

To solve a set of these equations, the three-dimensional MMA scheme treats eight dependent variables; the point value of the profile $f_{i,j,k}$ and the piecewise moments,

$$\boldsymbol{M}^m_{i+1/2,j+1/2,k+1/2} = \frac{1}{m!}\int_{z_k}^{z_{k+1}}\int_{y_j}^{y_{j+1}}\int_{x_i}^{x_{i+1}} \boldsymbol{x}^m f dV, \quad (m = 0, 1, 2)\,, \tag{10}$$

and constructs a piecewise interpolation for f in a cell with a quadratic polynominal,

$$F_{i,j,k}(x, y, z) = \sum_{\nu=1}^{3}\sum_{\mu=1}^{3}\sum_{\lambda=1}^{3} \nu\mu\lambda C_{\nu\mu\lambda;i,j,k}\,(x - x_i)^{\lambda-1}\,(y - y_j)^{\mu-1}\,(z - z_k)^{\nu-1}\,, \tag{11}$$

which gives an interpolation function for $\boldsymbol{M}^m$ as

$$\begin{aligned} \boldsymbol{G}^m_{i,j,k}(x, y, z) &= \frac{1}{m!}\int_{z_k}^{z}\int_{y_j}^{y}\int_{x_i}^{x} \boldsymbol{x'}^m F_{i,j,k}\left(x', y', z'\right) dV' \\ &= \sum_{\nu=1}^{3}\sum_{\mu=1}^{3}\sum_{\lambda=1}^{3} \begin{pmatrix} A^m_\lambda(x, x_i) \\ A^m_\mu(y, y_j) \\ A^m_\nu(z, z_k) \end{pmatrix} \\ &\quad \times C_{\nu\mu\lambda;i,j,k}\,(x - x_i)^\lambda\,(y - y_j)^\mu\,(z - z_k)^\nu\,, \quad (m = 0, 1, 2) \end{aligned} \tag{12}$$

where $\boldsymbol{G}^m = \left(G^m_x, G^m_y, G^m_z\right)$, $G^0_x = G^0_y = G^0_z = G^0$, and

$$\begin{cases} A^0_\lambda(x, x_i) &= 1, \\ A^1_\lambda(x, x_i) &= (\lambda x + x_i)/(\lambda + 1)\,, \\ A^2_\lambda(x, x_i) &= \left\{\frac{\lambda(\lambda+1)}{2}x^2 + \lambda x_i x + x_i^2\right\}/\left\{(\lambda + 1)(\lambda + 2)\right\}. \end{cases} \tag{13}$$

To determine the coefficients $C_{\nu\mu\lambda;i,j,k}$, we use the variables at the upwind

position as constraints,

$$\left\{\begin{array}{lcl} F_{i,j,k}\left(x_i,y_j,z_k\right) & = & f_{i,j,k}, \\ F_{i,j,k}\left(x_{iup},y_j,z_k\right) & = & f_{iup,j,k}, \\ F_{i,j,k}\left(x_i,y_{jup},z_k\right) & = & f_{i,jup,k}, \\ F_{i,j,k}\left(x_i,y_j,z_{kup}\right) & = & f_{i,j,kup}, \\ F_{i,j,k}\left(x_{iup},y_{jup},z_k\right) & = & f_{iup,jup,k}, \\ F_{i,j,k}\left(x_i,y_{jup},z_{kup}\right) & = & f_{i,jup,kup}, \\ F_{i,j,k}\left(x_{iup},y_j,z_{kup}\right) & = & f_{iup,j,kup}, \\ F_{i,j,k}\left(x_{iup},y_{jup},z_{kup}\right) & = & f_{iup,jup,kup}, \\ \boldsymbol{G}^m_{i,j,k}\left(x_{iup},y_{jup},z_{kup}\right) & = & \mathrm{sgn}\left(\zeta_{i,j,k}\right)\mathrm{sgn}\left(\eta_{i,j,k}\right)\mathrm{sgn}\left(\theta_{i,j,k}\right) \\ & & \times \boldsymbol{M}^m_{icell,jcell,kcell}, \quad (m=0,1,2), \end{array}\right. \tag{14}$$

where

$$\left\{\begin{array}{lcl} iup & = & i+\mathrm{sgn}\left(\zeta_{i,j,k}\right), \\ icell & = & i+\mathrm{sgn}\left(\zeta_{i,j,k}\right)/2, \\ jup & = & j+\mathrm{sgn}\left(\eta_{i,j,k}\right), \\ jcell & = & j+\mathrm{sgn}\left(\eta_{i,j,k}\right)/2, \\ kup & = & k+\mathrm{sgn}\left(\theta_{i,j,k}\right), \\ kcell & = & k+\mathrm{sgn}\left(\theta_{i,j,k}\right)/2, \end{array}\right. \tag{15}$$

are the position of the upwind grid and cell in the x, y, and z directions, $\mathrm{sgn}\left(\zeta\right)$ stands for the sign of ζ, and $\left(\zeta_{i,j,k},\eta_{i,j,k},\theta_{i,j,k}\right)$ is the distance of the upwind departure position relative to $\left(x_i,y_j,z_k\right)$, determined with a second order accuracy,

$$\left(\begin{array}{c} \zeta_{i,j,k} \\ \eta_{i,j,k} \\ \theta_{i,j,k} \end{array}\right) = -\boldsymbol{u}_{i,j,k}\Delta t + \left[\left(\boldsymbol{u}\cdot\nabla\right)\boldsymbol{u}\right]_{i,j,k}\frac{\Delta t^2}{2}.$$

Eq. (14) is obviously insufficient to determine the twenty-seven coefficients $C_{\nu\mu\lambda;i,j,k}$. Then, we additionally introduce line-integrated variables $\boldsymbol{l}=\left(l_x,l_y,l_z\right)$ defined as

$$l_{x;i+1/2,j,k}=\int_{x_i}^{x_{i+1}} f dx,\ l_{y;i,j+1/2,k}=\int_{y_j}^{y_{j+1}} f dy,\ l_{z;i,j,k+1/2}=\int_{z_k}^{z_{k+1}} f dz, \tag{16}$$

and use their upwind values as constraints,

$$\left\{\begin{array}{lcl} L_{x;i,j,k}\left(x_{iup},y_j,z_k\right) & = & \mathrm{sgn}\left(\zeta_{i,j,k}\right) l_{x;icell,j,k}, \\ L_{x;i,j,k}\left(x_{iup},y_{jup},z_k\right) & = & \mathrm{sgn}\left(\zeta_{i,j,k}\right) l_{x;icell,jup,k}, \\ L_{x;i,j,k}\left(x_{iup},y_j,z_{kup}\right) & = & \mathrm{sgn}\left(\zeta_{i,j,k}\right) l_{x;icell,j,kup}, \\ L_{x;i,j,k}\left(x_{iup},y_{jup},z_{kup}\right) & = & \mathrm{sgn}\left(\zeta_{i,j,k}\right) l_{x;icell,jup,kup}, \\ L_{y;i,j,k}\left(x_i,y_{jup},z_k\right) & = & \mathrm{sgn}\left(\eta_{i,j,k}\right) l_{y;i,jcell,k}, \\ L_{y;i,j,k}\left(x_i,y_{jup},z_{kup}\right) & = & \mathrm{sgn}\left(\eta_{i,j,k}\right) l_{y;i,jcell,kup}, \\ L_{y;i,j,k}\left(x_{iup},y_{jup},z_k\right) & = & \mathrm{sgn}\left(\eta_{i,j,k}\right) l_{y;iup,jcell,k}, \\ L_{y;i,j,k}\left(x_{iup},y_{jup},z_{kup}\right) & = & \mathrm{sgn}\left(\eta_{i,j,k}\right) l_{y;iup,jcell,kup}, \\ L_{z;i,j,k}\left(x_i,y_j,z_{kup}\right) & = & \mathrm{sgn}\left(\theta_{i,j,k}\right) l_{z;i,j,kcell}, \\ L_{z;i,j,k}\left(x_{iup},y_j,z_{kup}\right) & = & \mathrm{sgn}\left(\theta_{i,j,k}\right) l_{z;iup,j,kcell}, \\ L_{z;i,j,k}\left(x_i,y_{jup},z_{kup}\right) & = & \mathrm{sgn}\left(\theta_{i,j,k}\right) l_{z;i,jup,kcell}, \\ L_{z;i,j,k}\left(x_{iup},y_{jup},z_{kup}\right) & = & \mathrm{sgn}\left(\theta_{i,j,k}\right) l_{z;iup,jup,kcell}, \end{array}\right. \tag{17}$$

where

$$\begin{aligned} L_{x;i,j,k}\left(x,y,z\right) &= \int_{x_i}^{x} F_{i,j,k}\left(x',y,z\right) dx' \\ &= \sum_{\nu=1}^{3}\sum_{\mu=1}^{3}\sum_{\lambda=1}^{3} \nu\mu C_{\nu\mu\lambda;i,j,k}\left(x-x_i\right)^{\lambda}\left(y-y_j\right)^{\mu-1}\left(z-z_k\right)^{\nu-1}, \end{aligned} \tag{18}$$

and $L_{y;i,j,k}, L_{z;i,j,k}$ are given likewise. Consequently, the coefficients are explicitly determined, which are listed in Appendix A.

To save memory cost of our Vlasov simulation code, we do not treat the line-integrated variables as dependent variables. Therefore, they should be constructed from known variables. We find that a construction technique used in the Weighted ENO scheme (Jiang and Shu, 1996) works well for problems we are concerned. The line-integrated variable $l_{x;i+1/2}$ is constructed from four point values $(f_{i-1}, f_i, f_{i+1}, f_{i+2})$ as

$$\begin{aligned} l_{x;i+1/2} &= \frac{\Delta x\left[\alpha_L\left(-f_{i-1}+8f_i+5f_{i+1}\right)+\alpha_R\left(5f_i+8f_{i+1}-f_{i+2}\right)\right]}{12\left(\alpha_L+\alpha_R\right)}, \\ \alpha_{L,R} &= \left(IS_{L,R}+\epsilon\right)^{-p}, \end{aligned} \tag{19}$$

where we use $p=2$ and $\epsilon=10^{-6}$ (same as in Jiang and Shu (1996)), and a uniform grid spacing is assumed. Simulation results are not sensitive to the choice of p, ϵ. $IS_{L,R}$ is a smoothness measurement of the interpolation function $q_{L,R}\left(x\right)$ (second order polynominal) on the left- and right-side stencils,

$(i-1, i, i+1)$ and $(i, i+1, i+2)$, defined as

$$
\begin{aligned}
IS_{L,R} &= \Delta x \int_{x_i}^{x_{i+1}} \left[\left(\frac{\partial q_{L,R}}{\partial x} \right)^2 + \left(\Delta x \frac{\partial^2 q_{L,R}}{\partial x^2} \right)^2 \right] dx, \\
q_L(x) &= \frac{f_{i-1} - 2f_i + f_{i+1}}{2\Delta x^2} (x - x_i)^2 + \frac{f_{i+1} - f_{i-1}}{2\Delta x} (x - x_i) + f_i, \\
q_R(x) &= \frac{f_i - 2f_{i+1} + f_{i+2}}{2\Delta x^2} (x - x_{i+1})^2 + \frac{f_{i+2} - f_i}{2\Delta x} (x - x_{i+1}) + f_{i+1},
\end{aligned}
$$

giving

$$
\begin{aligned}
IS_L &= \frac{(f_{i-1} - 2f_i + f_{i+1})(5f_{i-1} - 16f_i + 11f_{i+1})}{6} + \frac{(f_{i+1} - f_{i-1})^2}{4}, \\
IS_R &= \frac{(f_i - 2f_{i+1} + f_{i+2})(11f_i - 16f_{i+1} + 5f_{i+2})}{6} + \frac{(f_{i+2} - f_i)^2}{4}.
\end{aligned}
$$

Eq. (19) gives a fourth-order central interpolation when $\alpha_L = \alpha_R$.

2.1. Time integration for the advection

Let us consider the time integration of the variables. For the Vlasov equation in magnetized plasma, we consider two problems of the advection with constant velocity and the solid body rotation. When the velocity is constant in space, we employ the semi-Lagrangian method. This method has been also applied to the one- and two-dimensional schemes. The advection phase of Eqs. (5)-(9) is calculated as

$$
\begin{aligned}
{}^{n+1}f_{i,j,k} &= {}^{n}F_{i,j,k}(x_i + \zeta, y_j + \eta, z_k + \theta), \qquad (20) \\
{}^{n+1}M^0_{icell,jcell,kcell} &= \mathrm{sgn}(\zeta)\,\mathrm{sgn}(\eta)\,\mathrm{sgn}(\theta) \\
&\quad \times \left[\int_{z_k+\theta}^{z_{kup}} \int_{y_j+\eta}^{y_{jup}} \int_{x_i+\zeta}^{x_{iup}} {}^{n}F_{i,j,k} dV \right. \\
&\quad + \int_{z_k+\theta}^{z_{kup}} \int_{y_j+\eta}^{y_{jup}} \int_{x_{iup}}^{x_{iup}+\zeta} {}^{n}F_{iup,j,k} dV \\
&\quad + \int_{z_k+\theta}^{z_{kup}} \int_{y_{jup}}^{y_{jup}+\eta} \int_{x_i+\zeta}^{x_{iup}} {}^{n}F_{i,jup,k} dV \\
&\quad + \int_{z_{kup}}^{z_{kup}+\theta} \int_{y_j+\eta}^{y_{jup}} \int_{x_i+\zeta}^{x_{iup}} {}^{n}F_{i,j,kup} dV \\
&\quad + \int_{z_k+\theta}^{z_{kup}} \int_{y_{jup}}^{y_{jup}+\eta} \int_{x_{iup}}^{x_{iup}+\zeta} {}^{n}F_{iup,jup,k} dV \\
&\quad + \int_{z_{kup}}^{z_{kup}+\theta} \int_{y_{jup}}^{y_{jup}+\eta} \int_{x_i+\zeta}^{x_{iup}} {}^{n}F_{i,jup,kup} dV \\
&\quad \left. + \int_{z_{kup}}^{z_{kup}+\theta} \int_{y_j+\eta}^{y_{jup}} \int_{x_{iup}}^{x_{iup}+\zeta} {}^{n}F_{iup,j,kup} dV \right.
\end{aligned}
$$

$$+\int_{z_{kup}}^{z_{kup}+\theta}\int_{y_{jup}}^{y_{jup}+\eta}\int_{x_{iup}}^{x_{iup}+\zeta} {}^{n}F_{iup,jup,kup}dV\Bigg], \tag{21}$$

$$\begin{aligned}
{}^{*}\boldsymbol{M}^{m}_{icell,jcell,kcell} &= \frac{\mathrm{sgn}\,(\zeta)\,\mathrm{sgn}\,(\eta)\,\mathrm{sgn}\,(\theta)}{m!} \\
&\times\Bigg[\int_{z_k+\theta}^{z_{kup}}\int_{y_j+\eta}^{y_{jup}}\int_{x_i+\zeta}^{x_{iup}} \boldsymbol{x}^m\cdot{}^{n}F_{i,j,k}dV \\
&+\int_{z_k+\theta}^{z_{kup}}\int_{y_j+\eta}^{y_{jup}}\int_{x_{iup}}^{x_{iup}+\zeta} \boldsymbol{x}^m\cdot{}^{n}F_{iup,j,k}dV \\
&+\int_{z_k+\theta}^{z_{kup}}\int_{y_{jup}}^{y_{jup}+\eta}\int_{x_i+\zeta}^{x_{iup}} \boldsymbol{x}^m\cdot{}^{n}F_{i,jup,k}dV \\
&+\int_{z_{kup}}^{z_{kup}+\theta}\int_{y_j+\eta}^{y_{jup}}\int_{x_i+\zeta}^{x_{iup}} \boldsymbol{x}^m\cdot{}^{n}F_{i,j,kup}dV \\
&+\int_{z_k+\theta}^{z_{kup}}\int_{y_{jup}}^{y_{jup}+\eta}\int_{x_{iup}}^{x_{iup}+\zeta} \boldsymbol{x}^m\cdot{}^{n}F_{iup,jup,k}dV \\
&+\int_{z_{kup}}^{z_{kup}+\theta}\int_{y_{jup}}^{y_{jup}+\eta}\int_{x_i+\zeta}^{x_{iup}} \boldsymbol{x}^m\cdot{}^{n}F_{i,jup,kup}dV \\
&+\int_{z_{kup}}^{z_{kup}+\theta}\int_{y_j+\eta}^{y_{jup}}\int_{x_{iup}}^{x_{iup}+\zeta} \boldsymbol{x}^m\cdot{}^{n}F_{iup,j,kup}dV \\
&+\int_{z_{kup}}^{z_{kup}+\theta}\int_{y_{jup}}^{y_{jup}+\eta}\int_{x_{iup}}^{x_{iup}+\zeta} \boldsymbol{x}^m\cdot{}^{n}F_{iup,jup,kup}dV\Bigg], \quad (m=1,2), \qquad (22)
\end{aligned}$$

where the left-superscript indicates the number of time steps and the asterisk means that the variables are at the intermediate step. Here, we consider the case of the CFL number $|u\Delta t/\Delta x|, |v\Delta t/\Delta y|, |w\Delta t/\Delta z| < 1$ for simplicity. Integrations on the right-hand side of Eqs. (21) and (22) can be exactly calculated by using Eq. (12). Next, we advance the non-advection phase of Eqs. (7)-(9) as

$${}^{n+1}\boldsymbol{M}^{1}_{i+1/2,j+1/2,k+1/2} = {}^{*}\boldsymbol{M}^{1}_{i+1/2,j+1/2,k+1/2} + {}^{n+1}M^{0}_{i+1/2,j+1/2,k+1/2}\boldsymbol{u}\Delta t, \tag{23}$$

$$\begin{aligned}
{}^{n+1}\boldsymbol{M}^{2}_{i+1/2,j+1/2,k+1/2} &= {}^{*}\boldsymbol{M}^{2}_{i+1/2,j+1/2,k+1/2} \\
&+\left({}^{*}\boldsymbol{M}^{1}_{i+1/2,j+1/2,k+1/2} + {}^{n+1}M^{0}_{i+1/2,j+1/2,k+1/2}\frac{\boldsymbol{u}\Delta t}{2}\right)\boldsymbol{u}\Delta t. \qquad (24)
\end{aligned}$$

2.2. Time integration for the solid body rotation

When the velocity varies in space (including the solid body rotation problem), we employ a time integration method proposed by Ii and Xiao (2007), in which cell-integrated values are advanced by the finite volume method with the Runge-Kutta time integration, whereas point values are advanced by the semi-Lagrangian method. This method has been also applied to the two-dimensional scheme.

In the three-dimensional solid body rotation problem, the velocity is generally given as $(u, v, w) = (y\omega_z - z\omega_y, z\omega_x - x\omega_z, x\omega_y - y\omega_x)$, where $\boldsymbol{\omega} = (\omega_x, \omega_y, \omega_z)$ is the angular velocity. With an arbitrary $\boldsymbol{\omega}$, the rotation axis passes through simulation cells with an arbitrary angle, causing the velocity reversal within a single cell. This is an unfavorable situation for conservative-form upwind schemes. To avoid this situation, we split it into two phases, $(u, v, w) = (y\omega_z, z\omega_x, x\omega_y)$ and $(-z\omega_y, -x\omega_z, -y\omega_x)$, and then alternately advance.

At the first phase, Eqs. (6)-(9) are approximated into the following finite volume formulation,

$$\begin{aligned}
\frac{\partial M^0_{i+1/2,j+1/2,k+1/2}}{\partial t} &= -y_{j+1/2}\omega_z \partial_x \left(\int\int f dy dz \right)_{i+1/2,j+1/2,k+1/2} \\
&\quad -z_{k+1/2}\omega_x \partial_y \left(\int\int f dz dx \right)_{i+1/2,j+1/2,k+1/2} \\
&\quad -x_{i+1/2}\omega_y \partial_z \left(\int\int f dx dy \right)_{i+1/2,j+1/2,k+1/2}, \qquad (25) \\
\frac{\partial \boldsymbol{M}^m_{i+1/2,j+1/2,k+1/2}}{\partial t} &= -\frac{y_{j+1/2}\omega_z}{m!} \partial_x \left(\int\int \boldsymbol{x}^m f dy dz \right)_{i+1/2,j+1/2,k+1/2} \\
&\quad -\frac{z_{k+1/2}\omega_x}{m!} \partial_y \left(\int\int \boldsymbol{x}^m f dz dx \right)_{i+1/2,j+1/2,k+1/2} \\
&\quad -\frac{x_{i+1/2}\omega_y}{m!} \partial_z \left(\int\int \boldsymbol{x}^m f dx dy \right)_{i+1/2,j+1/2,k+1/2} \\
&\quad + \begin{pmatrix} y_{j+1/2}\omega_z M^{m-1}_{x;i+1/2,j+1/2,k+1/2} \\ z_{k+1/2}\omega_x M^{m-1}_{y;i+1/2,j+1/2,k+1/2} \\ x_{i+1/2}\omega_y M^{m-1}_{z;i+1/2,j+1/2,k+1/2} \end{pmatrix}, \quad (m = 1, 2) \qquad (26)
\end{aligned}$$

where $\partial_x f_{i+1/2,j,k} = f_{i+1,j,k} - f_{i,j,k}$. Eq. (25) guarantees the conservation of mass. Area-integrated variables of f appearing on the right-hand side of Eqs. (25) and (26) are constructed from the interpolation function such as

$$\begin{aligned}
\left(\frac{1}{m!} \int\int x^m f dx dy \right)_{icell,jcell,k} &= \frac{\operatorname{sgn}(\zeta_{i,j,k}) \operatorname{sgn}(\eta_{i,j,k})}{m!} \int_{y_j}^{y_{jup}} \int_{x_i}^{x_{iup}} x^m F_{i,j,k}(x, y, z_k) \, dx dy \\
&= \operatorname{sgn}(\zeta_{i,j,k}) \operatorname{sgn}(\eta_{i,j,k}) \\
&\quad \times \sum_{\mu=1}^{3} \sum_{\lambda=1}^{3} A^m_\lambda (x_{iup}, x_i) \, C_{1\mu\lambda;i,j,k} \Delta x^\lambda \Delta y^\mu, \quad (m = 0, 1, 2),
\end{aligned}$$

where $\Delta x = x_{iup} - x_i$ and $\Delta y = y_{jup} - y_j$.

For stable calculation, the time integration of Eqs. (25) and (26) is implemented with the third-order TVD Runge-Kutta method (Shu and Osher, 1988; Gottlieb and Shu, 1998). Intermediate values of f at each stage, which are necessary to calculate the coefficients of the interpolation function, are approximated by solving the equation of the characteristics with the Runge-Kutta method,

$$\frac{d}{dt}\begin{pmatrix}\zeta_{i,j,k}\\ \eta_{i,j,k}\\ \theta_{i,j,k}\end{pmatrix} = \begin{pmatrix}\{y_j+\eta_{i,j,k}\}\,\omega_z\\ \{z_k+\theta_{i,j,k}\}\,\omega_x\\ \{x_i+\zeta_{i,j,k}\}\,\omega_y\end{pmatrix}, \quad \begin{pmatrix}{}^0\zeta_{i,j,k}\\ {}^0\eta_{i,j,k}\\ {}^0\theta_{i,j,k}\end{pmatrix} = 0,$$
$${}^s f_{i,j,k} = {}^n F_{i,j,k}\left(x_i+{}^s\zeta_{i,j,k}, y_j+{}^s\eta_{i,j,k}, z_k+{}^s\theta_{i,j,k}\right), \tag{27}$$

where the left-superscript $s = 0, 1, 2, 3$ denotes the Runge-Kutta stage. The point value is advanced by ${}^* f_{i,j,k} = {}^3 f_{i,j,k}$.

In addition, we should calculate intermediate values of $\boldsymbol{l}$ at each stage, which are also necessary to calculate the coefficients. Integrating Eq. (5) over x, the governing equation of l_x is approximated as

$$\frac{\partial l_x}{\partial t} + \int dx \frac{\partial}{\partial x}(uf) + v\frac{\partial l_x}{\partial y} + w\frac{\partial l_x}{\partial z} = 0.$$

The second term is advanced by the finite volume method, and third and fourth terms are advanced by the semi-Lagrangian method. The solutions at stages are approximated as

$$\begin{aligned}
{}^1 l_{x,icell,j,k} &= \mathrm{sgn}\left(\zeta_{i,j,k}\right) {}^n L_{x;i,j,k}\left(x_{iup}, y_j+{}^1\eta_{icell,j,k}, z_k+{}^1\theta_{icell,j,k}\right)\\
&\quad -y_j\omega_z\Delta t\partial_x {}^0 f_{icell,j,k},\\
{}^2 l_{x,icell,j,k} &= \mathrm{sgn}\left(\zeta_{i,j,k}\right) {}^n L_{x;i,j,k}\left(x_{iup}, y_j+{}^2\eta_{icell,j,k}, z_k+{}^2\theta_{icell,j,k}\right)\\
&\quad -y_j\omega_z\Delta t\frac{\partial_x\left({}^0 f+{}^1 f\right)_{icell,j,k}}{4},\\
{}^* l_{x,icell,j,k} &= \mathrm{sgn}\left(\zeta_{i,j,k}\right) {}^n L_{x;i,j,k}\left(x_{iup}, y_j+{}^3\eta_{icell,j,k}, z_k+{}^3\theta_{icell,j,k}\right)\\
&\quad -y_j\omega_z\Delta t\frac{\partial_x\left({}^0 f+{}^1 f+4{}^2 f\right)_{icell,j,k}}{6},
\end{aligned}$$

and l_y, l_z are approximated likewise.

Consequently, we can calculate the coefficients at each stage, and then advance the moments with the Runge-Kutta method, which is implemented as follows,

$${}^1\boldsymbol{M}^m = {}^n\boldsymbol{M}^m + \boldsymbol{R}({}^n f, {}^n\boldsymbol{l}, {}^n\boldsymbol{M}^m)\Delta t,$$

$$
\begin{aligned}
{}^2\boldsymbol{M}^m &= \frac{3}{4}{}^n\boldsymbol{M}^m + \frac{1}{4}\left\{{}^1\boldsymbol{M}^m + \boldsymbol{R}({}^1f, {}^1\boldsymbol{l}, {}^1\boldsymbol{M}^m)\Delta t\right\}, \\
{}^*\boldsymbol{M}^m &= \frac{1}{3}{}^n\boldsymbol{M}^m + \frac{2}{3}\left\{{}^2\boldsymbol{M}^m + \boldsymbol{R}({}^2f, {}^2\boldsymbol{l}, {}^2\boldsymbol{M}^m)\Delta t\right\}, \quad (m = 0, 1, 2), \qquad (28)
\end{aligned}
$$

where $\boldsymbol{R}$ stands for the right-hand side of Eqs. (25) and (26).

The second phase is advanced in a similar way. The time integration of the whole system is carried out with three steps; a half time step at the first phase $({}^nf, {}^n\boldsymbol{M}) \to ({}^*f, {}^*\boldsymbol{M})$, a full time step at the second phase $({}^*f, {}^*\boldsymbol{M}) \to ({}^{**}f, {}^{**}\boldsymbol{M})$, and then a half time step at the first phase $({}^{**}f, {}^{**}\boldsymbol{M}) \to ({}^{n+1}f, {}^{n+1}\boldsymbol{M})$.

3. Benchmark tests

As a benchmark test, we simulate the long time solid body rotation and advection problem,

$$
\frac{\partial f}{\partial t} + \{(\boldsymbol{x} - \boldsymbol{x_0}) \times \boldsymbol{\omega}\} \cdot \frac{\partial f}{\partial \boldsymbol{x}} = 0, \qquad (29)
$$

of a gaussian profile,

$$
f\left(x, y, z, t = 0\right) = \exp\left[-\left\{\frac{\left(x - x_0\right)^2}{2\sigma_x^2} + \frac{\left(y - y_0\right)^2}{2\sigma_y^2} + \frac{\left(z - z_0\right)^2}{2\sigma_z^2}\right\}\right]. \qquad (30)
$$

This equation describes the rotation around $(x, y, z) = (x_0, y_0, z_0)$. To solve the equation, we split it into the rotation and advection phases, and advance them as follows; the advection with a half time step, the rotation with a full time step (this includes three steps), and then the advection with a half time step. The angular velocity is $(\omega_x, \omega_y, \omega_z) = (1/\sqrt{6}, 1/\sqrt{3}, 1/\sqrt{2})$. The simulation domain is $[-1, 1]$ with 32 grid points in each direction. The open boundary condition is employed where constant incoming fluxes are assumed while outgoing fluxes are perfectly lost. The time step is $2\pi/750$. The simulation runs till hundred rotation periods. We compare the results with the CIP-CSL2 scheme (Takizawa et al., 2002). Note that both the MMA and CIP-CSL2 schemes treat eight dependent variables in three dimension.

Fig. 1 shows the results for a symmetric gaussian profile with $\sigma_x = \sigma_y = \sigma_z = 0.2, x_0 = y_0 = z_0 = 0$ (without the advection). Compared to the CIP-CSL2 scheme (c), the MMA scheme (b) completely preserves the profile even after a hundred of rotations. From these simulation runs with different grid sizes, we evaluate the order of accuracy of the schemes. Fig. 2 shows

the error $\sum_{i,j,k} |f(x,y,z,t) - f(x,y,z,0)|/N$ as a function of the grid size (N is the number of grid points). Both schemes show nearly the third order accuracy in space (dashed line). The error of the MMA scheme (triangles) is $\sim 10^{-1.5}$ times smaller than the CIP-CSL2 scheme (diamonds). With the finest grid size, the accuracy of the MMA scheme is slightly worse than the third order. Currently, we cannot identify its cause.

Fig. 3 shows the results for an asymmetric gaussian profile with $\sigma_x = 0.15, \sigma_y = 0.2, \sigma_z = 0.25, x_0 = y_0 = z_0 = 0$ (without the advection). By fitting the profile with the gaussian function, Fig. 4 shows the temporal variation of the standard deviation $(\sigma_x, \sigma_y, \sigma_z)$. While the CIP-CSL2 scheme shows the rapid increase due to numerical diffusion, the MMA scheme keeps the standard deviation with small errors. The smallest deviation σ_x (a) slightly increases, whereas others (b,c) decrease. However, their average (d) is kept constant.

Fig. 5 shows the results for a symmetric gaussian profile with $\sigma_x = \sigma_y = \sigma_z = 0.2, x_0 = 0.2, y_0 = 0.15, z_0 = -0.1$. The MMA scheme provides a better solution with keeping $(\sigma_x, \sigma_y, \sigma_z)$ and (x_0, y_0, z_0) constant, indicating that the scheme can accurately solve the electric field $(\boldsymbol{E} \times \boldsymbol{B})$ drift motion with little numerical dispersion or heating. Hence, the three-dimensional MMA scheme is a very suitable method for long time Vlasov simulations of magnetized plasma.

4. Electromagnetic Vlasov simulations

We apply the three-dimensional MMA scheme to electromagnetic Vlasov-Maxwell simulations. The one-dimensional electromagnetic Vlasov-Maxwell system of equations is written as

$$\frac{\partial f_s}{\partial t} + v_x \frac{\partial f_s}{\partial x} + \frac{q_s}{m_s}\left(\boldsymbol{E} + \frac{\boldsymbol{v} \times \boldsymbol{B}}{c}\right) \cdot \frac{\partial f_s}{\partial \boldsymbol{v}} = 0, \quad (s = p, e)\,, \tag{31}$$

$$\frac{\partial \boldsymbol{E}}{\partial t} = c\nabla \times \boldsymbol{B} - 4\pi \boldsymbol{j}, \quad \frac{\partial \boldsymbol{B}}{\partial t} = -c\nabla \times \boldsymbol{E}, \quad \boldsymbol{j} = \sum_{s=p,e} q_s \int \boldsymbol{v} f_s d\boldsymbol{v}, \tag{32}$$

where $\boldsymbol{E}(x)$ and $\boldsymbol{B}(x)$ are the electric and magnetic fields, $\boldsymbol{j}(x)$ is the current density, c is the speed of light, q_s is the charge, m_s is the mass, $f_s(\boldsymbol{v}, x)$ is the phase space distribution function, and the subscript s denotes particle species (p for protons and e for electrons). Although configuration space is

assumed one dimension, full three-dimensional velocity space and electromagnetic fields are treated.

In the simulation, we treat sixteen dependent variables for both electrons and protons; point values of the distribution function, piecewise moments in the velocity space, and their cell-integrated values in the configuration space,

$$
\begin{aligned}
&f_{i,j,k,l} = f\left(v_{x;i}, v_{y;j}, v_{z;k}, x_l\right), \\
&\boldsymbol{M}^m_{i+1/2,j+1/2,k+1/2,l} = \frac{1}{m!}\int_{v_{z;k}}^{v_{z;k+1}}\int_{v_{y;j}}^{v_{y;j+1}}\int_{v_{x;i}}^{v_{x;i+1}} \boldsymbol{v}^m f\left(\boldsymbol{v}, x_l\right) d\boldsymbol{v}, \\
&\tilde{f}_{i,j,k,l+1/2} = \int_{x_l}^{x_{l+1}} f\left(v_{x;i}, v_{y;j}, v_{z;k}, x\right) dx, \\
&\tilde{\boldsymbol{M}}^m_{i+1/2,j+1/2,k+1/2,l+1/2} = \frac{1}{m!}\int_{x_l}^{x_{l+1}}\int_{v_{z;k}}^{v_{z;k+1}}\int_{v_{y;j}}^{v_{y;j+1}}\int_{v_{x;i}}^{v_{x;i+1}} \boldsymbol{v}^m f\left(\boldsymbol{v}, x\right) d\boldsymbol{v}dx,
\end{aligned}
$$

where the subscripts i, j, k, and l denote the grid position in the v_x, v_y, v_z, and x directions, $\boldsymbol{M}^m = (M^m_{v_x}, M^m_{v_y}, M^m_{v_z})$, $M^0_{v_x} = M^0_{v_y} = M^0_{v_z} = M^0$, $\tilde{\boldsymbol{M}}^m = (\tilde{M}^m_{v_x}, \tilde{M}^m_{v_y}, \tilde{M}^m_{v_z})$, $\tilde{M}^0_{v_x} = \tilde{M}^0_{v_y} = \tilde{M}^0_{v_z} = \tilde{M}^0$, and $m = 0, 1, 2$. We split the Vlasov equation (31) into two equations in three-dimensional velocity and one-dimensional configuration spaces, which are alternately advanced by the MMA scheme and the CIP-CSL2 scheme (Yabe et al., 2001), respectively. The Maxwell equation (32) is solved by the implicit scheme (Hoshino, 1986, 1987). The time integration of the system is carried out in the same manner as Minoshima et al. (2011). Physical variables in the system are normalized as follows; velocity by the speed of light, time by the inverse electron plasma frequency ω_{pe}, electromagnetic fields by an ambient magnetic field strength, and position by the Debye length λ_D. The boundary conditions are periodic in the configuration space and open in the velocity space where constant incoming fluxes are assumed while outgoing fluxes are perfectly lost. The simulations are executed on a generic workstation with dual Intel Xeon Quad-Core processors.

4.1. Perpendicular wave propagation

We first test the linear wave propagation perpendicular to the magnetic field line, which has been previously tested in Minoshima et al. (2011) (in the paper, we assumed two dimensionality in velocity space). Since the three-dimensional scheme is not designed in the same way as the two-dimensional one, we test the same problem again. The initial plasma condition is a

uniform and isotropic Maxwell distribution with a small (1%) uniform random perturbation only for the electron density. A uniform magnetic field is initially imposed in the z-direction. The initial electric field is determined from the Poisson equation (Gauss's law). Simulation parameters are as follows; a mass ratio $m_p/m_e = 16$, a ratio of the electron gyro to plasma frequency $\omega_{ge}/\omega_{pe} = 0.5$, and electron and proton thermal velocities $v_{e;th} = 0.1, v_{p;th} = 0.025$, corresponding to electron and proton plasma beta values being $\beta_e = \beta_p = 0.04$. The simulation domain in the velocity space is $[-4v_{th}, 4v_{th}]$ with 32 grid points in each direction for each species. The grid size in the configuration space is equal to λ_D, and the spatial length is $512\lambda_D$. The time step is $0.05/\sqrt{2}\omega_{pe}^{-1}$.

Fig. 6 shows the Fourier spectrum of the electrostatic field E_x integrated until (a) $\omega_{pe}t = 361.3$ and (b) $\omega_{pe}t = 723.4$. Similar to the previous simulation, we can clearly identify the electron and ion cyclotron (Bernstein) modes, X- and Z-modes, and lower-hybrid waves. During the simulation (electrons gyrate more than fifty times), the total energy is conserved within an error of 0.1%.

4.2. Parallel wave propagation

We next test the linear wave propagation parallel to the magnetic field line. The initial plasma condition is a uniform and isotropic Maxwell distribution. A uniform magnetic field is initially imposed in the x-direction, and then a small (1%) uniform random perturbation is added to the transverse field. The initial electric field is zero. Simulation parameters are the same as in Section 4.1. The simulation domain in the velocity space is $[-4v_{th}, 4v_{th}]$ with 32 grid points in each direction for each species. The grid size in the configuration space is $4\lambda_D$, and the spatial length is $2048\lambda_D$. The time step is $0.1/\sqrt{2}\omega_{pe}^{-1}$.

Fig. 7(a) shows the Fourier spectrum of the transverse field B_y integrated until $\omega_{pe}t = 723.4$. For comparison, we also perform the electromagnetic PIC simulation with the same parameters (except that the grid size is λ_D in the PIC), and the result is shown in Fig. 7(b). The number of particles in each cell is 12,500 so that the total memory usage is comparable between the two simulations. We can clearly identify the R- and L-modes, and whistler waves. The ion-cyclotron wave is not clear because the integration time is not sufficiently long. During the Vlasov simulation, the total energy is conserved within an error of 0.005%.

The high frequency whistler waves ($\omega \gtrsim -kv_{e;th}+\omega_{ge}$) effectively dissipate in the Vlasov simulation through the cyclotron damping by thermal electrons, while it is not clear in the PIC simulation owing to the thermal noise.

4.3. Electron temperature anisotropy instability

We lastly test the nonlinear evolution of whistler waves through the electron temperature anisotropy instability (Sydora et al., 2007). The initial condition is a uniform and isotropic Maxwell distribution for protons, and bi-Maxwell distribution for electrons with a temperature anisotropy $T_{e\perp}/T_{e\parallel} > 1$, where $T_{e\perp}$ and $T_{e\parallel}$ are temperatures perpendicular and parallel to the magnetic field line. A uniform magnetic field is initially imposed in the x-direction, and then a uniform random perturbation is added to the transverse field to initiate the instability. The initial electric field is zero. Simulation parameters are as follows (same as in Sydora et al. (2007)): $m_p/m_e = 1836$, $\omega_{ge}/\omega_{pe} = 0.2$, $\beta_{e\parallel} = \beta_p = 1$, and $T_{e\perp}/T_{e\parallel} = 3$. The actual mass ratio is employed because protons do not play an important role in this instability. The simulation domain in the velocity space is $[-4.5v_{e;th}, 4.5v_{e;th}]$ for electrons, and $[-3v_{p;th}, 3v_{p;th}]$ for protons with 32 grid points in each direction. The grid size in the configuration space is $\Delta x = 4\lambda_D$, and the spatial length is $L = 2048\lambda_D$. The time step is $0.25/\sqrt{2}\omega_{pe}^{-1}$.

Fig. 8(a,b) shows the time profile of the transverse electric field spectrum $E_z(k,t)$ and distribution $E_z(x,t)$. At the linear phase, we observe wide-band waves in the wavenumber range of $kc/\omega_{pe} = 0.5 - 1.0$. During the nonlinear phase, the wavelength shifts to longer one ($kc/\omega_{pe} = 0.3 - 0.4$), and nearly coherent waves propagate forward and backward. These features are in good agreement with Sydora et al. (2007). Fig. 8(c) shows the Fourier spectrum of the transverse electric field $E_z(k,\omega)$ superimposed on the linear dispersion relation of the whistler wave (dashed line). The excited waves are certainly the whistler waves. Fig. 8(d) shows the time profile of E_z at the wavenumber corresponding to the fastest growing mode ($kc/\omega_{pe} = 0.7$). The growth rate agrees with the linear theory (Gurnett and Bhattacharjee (2005)).

Fig. 9(a,b) shows the longitudinal electron distribution function $\iint f_e dv_y dv_z$ at linear and nonlinear phases. The instability increases the electron temperature parallel to the ambient magnetic field line. Fig. 9(c) shows the time profile of the spatially-averaged perpendicular temperature $T_{e\perp} = (T_{ey} + T_{ez})/2$, parallel temperature $T_{e\parallel} = T_{ex}$, and temperature anisotropy $T_{e\perp}/T_{e\parallel}$. The temperature anisotropy is decreased as the electric field is increased (see, Fig. 8(d)). At the nonlinear phase, the system reaches marginal stability.

The saturation level of the temperature anisotropy $T_{e\perp}/T_{e\parallel} \simeq 1.2$ is in good agreement with Sydora et al. (2007). Fig. 9(d) shows the time profile of the total energy with different spatial resolution $(\Delta x, L)$. A black line shows the reference result $(4\lambda_D, 2048\lambda_D)$, a red line with finer grid size and narrower length $(\lambda_D, 512\lambda_D)$, and a blue line with narrower length $(4\lambda_D, 512\lambda_D)$. The total energy is slightly increased by 1.6%. The error level is not dependent on the spatial resolution. Therefore, we consider that the error is mainly caused by an inaccuracy of the distribution function in velocity space.

5. Summary and discussion

We have presented an extension of the multi-moment advection (MMA) scheme (Minoshima et al., 2011) to the three-dimensional case, for full electromagnetic Vlasov simulations of magnetized plasma. The scheme treats not only point values of a profile but also its zeroth to second order piecewise moments as dependent variables, and advances them on the basis of their governing equations. Similar to the one- and two-dimensional schemes, the three-dimensional scheme has quite high capability for Vlasov simulations.

The scheme is applied to the linear and nonlinear electromagnetic Vlasov simulations. Since the scheme can solve the solid body rotation and advection problem with little numerical dispersion or diffusion, it enables us to perform long time Vlasov simulations of magnetized plasma with small numerical errors. In the electron temperature anisotropy instability (Section 4.3), our Vlasov simulation code successfully describes the cooling as well as heating processes and the marginally stable state, by virtue of the diffusionless property of the scheme.

In this scheme, we apply the Weighted ENO construction technique for line-integrated variables (eq. (19)). This does not mean that the scheme possesses the non-oscillatory property. Better techniques may be devised to suppress numerical oscillations.

In the solid body rotation problem (Section 2.2), we split the velocity into two phases. Since the order of the first and second phases is arbitrary, a simulation result is not necessarily same when one reverses the order. However, we confirm that the effect is negligible small.

As shown in Minoshima et al. (2011), the one- and two-dimensional MMA schemes exactly guarantee the conservation of the zeroth to second order central moments in the advection problem with constant velocity, and the conservation of the sum of the second order moments in the solid body rotation

problem. The same holds for the tree-dimensional scheme in the advection problem, however, not in the solid body rotation problem, owing to the splitting procedure. Nevertheless, benchmark tests have shown that the scheme preserves the profile and the orbit of rotation with high accuracy.

One of advantages of the Vlasov simulation against the (explicit) PIC simulation is that the grid size in configuration space is not necessarily restricted to the Debye length. In fact, we set the grid size larger than the Debye length in Sections 4.2 and 4.3. This advantage can be applied especially to the simulation with the large frequency ratio ($\omega_{pe}/\omega_{ge} \gg 1$). Due to the restriction of the grid size, the frequency ratio ω_{pe}/ω_{ge} in many explicit PIC simulations is much smaller than in our space environment, to save computational cost. The Vlasov simulation can be performed with larger ω_{pe}/ω_{ge} within reasonable computational cost by using a coarser grid, unless Debye-scale structures are important. Therefore, our Vlasov simulation code will be able to simulate large-scale and long-time plasma kinetic phenomena with large ω_{pe}/ω_{ge}. Another advantage of the Vlasov simulation is the simplicity for parallel computation, because both the plasma and electromagnetic fields are treated as Eulerian variables. In these points of view, the Vlasov simulation is a necessary technique for the plasma kinetic simulation on present peta-scale and future exa-scale supercomputer systems.

Acknowledgements

T. M. is supported by a Grand-in-Aid for Young Scientists, (B) #21740135.

Appendix A. Coefficients of the interpolation function of MMA3D

$$C_{111;i,j,k} = f_{i,j,k}, \tag{A.1}$$

$$C_{112;i,j,k} = \frac{-1}{\Delta x}\left[2f_{i,j,k} + f_{iup,j,k} - \frac{3\mathrm{sgn}(\zeta_{i,j,k})}{\Delta x} l_{x;icell,j,k}\right], \tag{A.2}$$

$$C_{113;i,j,k} = \frac{1}{\Delta x^2}\left[f_{i,j,k} + f_{iup,j,k} - \frac{2\mathrm{sgn}(\zeta_{i,j,k})}{\Delta x} l_{x;icell,j,k}\right], \tag{A.3}$$

$$\begin{aligned} C_{122;i,j,k} = {} & \frac{1}{\Delta x \Delta y}\left[4f_{i,j,k} + 2\left(f_{iup,j,k} + f_{i,jup,k}\right) + f_{iup,jup,k}\right. \\ & -\frac{3\mathrm{sgn}(\zeta_{i,j,k})}{\Delta x}\left(2l_{x;icell,j,k} + l_{x;icell,jup,k}\right) \\ & \left.-\frac{3\mathrm{sgn}(\eta_{i,j,k})}{\Delta y}\left(2l_{y;i,jcell,k} + l_{y;iup,jcell,k}\right)\right] \end{aligned}$$

$$+\frac{27\mathrm{sgn}(\zeta_{i,j,k})\mathrm{sgn}(\eta_{i,j,k})\mathrm{sgn}(\theta_{i,j,k})}{\Delta x\Delta y\Delta z}H_{1z;i,j,k}\Big], \tag{A.4}$$

$$\begin{aligned}
C_{123;i,j,k} &= \frac{-1}{\Delta x^2\Delta y}\left[2\left(f_{i,j,k}+f_{iup,j,k}\right)+f_{i,jup,k}+f_{iup,jup,k}\right.\\
&-\frac{2\mathrm{sgn}(\zeta_{i,j,k})}{\Delta x}\left(2l_{x;icell,j,k}+l_{x;icell,jup,k}\right)\\
&-\frac{3\mathrm{sgn}(\eta_{i,j,k})}{\Delta y}\left(l_{y;i,jcell,k}+l_{y;iup,jcell,k}\right)\\
&\left.+\frac{18\mathrm{sgn}(\zeta_{i,j,k})\mathrm{sgn}(\eta_{i,j,k})\mathrm{sgn}(\theta_{i,j,k})}{\Delta x\Delta y\Delta z}H_{1z;i,j,k}\right],
\end{aligned} \tag{A.5}$$

$$\begin{aligned}
C_{133;i,j,k} &= \frac{1}{\Delta x^2\Delta y^2}\left[f_{i,j,k}+f_{iup,j,k}+f_{i,jup,k}+f_{iup,jup,k}\right.\\
&-\frac{2\mathrm{sgn}(\zeta_{i,j,k})}{\Delta x}\left(l_{x;icell,j,k}+l_{x;icell,jup,k}\right)\\
&-\frac{2\mathrm{sgn}(\eta_{i,j,k})}{\Delta y}\left(l_{y;i,jcell,k}+l_{y;iup,jcell,k}\right)\\
&\left.+\frac{12\mathrm{sgn}(\zeta_{i,j,k})\mathrm{sgn}(\eta_{i,j,k})\mathrm{sgn}(\theta_{i,j,k})}{\Delta x\Delta y\Delta z}H_{1z;i,j,k}\right],
\end{aligned} \tag{A.6}$$

$$\begin{aligned}
C_{222;i,j,k} &= \frac{-1}{\Delta x\Delta y\Delta z}\left[8f_{i,j,k}+4\left(f_{iup,j,k}+f_{i,jup,k}+f_{i,j,kup}\right)\right.\\
&+2\left(f_{iup,jup,k}+f_{i,jup,kup}+f_{iup,j,kup}\right)+f_{iup,jup,kup}\\
&-\frac{3\mathrm{sgn}(\zeta_{i,j,k})}{\Delta x}\left\{4l_{x;icell,j,k}+2\left(l_{x;icell,jup,k}+l_{x;icell,j,kup}\right)+l_{x;icell,jup,kup}\right\}\\
&-\frac{3\mathrm{sgn}(\eta_{i,j,k})}{\Delta y}\left\{4l_{y;i,jcell,k}+2\left(l_{y;i,jcell,kup}+l_{y;iup,jcell,k}\right)+l_{y;iup,jcell,kup}\right\}\\
&-\frac{3\mathrm{sgn}(\theta_{i,j,k})}{\Delta z}\left\{4l_{z;i,j,kcell}+2\left(l_{z;iup,j,kcell}+l_{z;i,jup,kcell}\right)+l_{z;iup,jup,kcell}\right\}\\
&+\frac{54\mathrm{sgn}(\zeta_{i,j,k})\mathrm{sgn}(\eta_{i,j,k})\mathrm{sgn}(\theta_{i,j,k})}{\Delta x\Delta y\Delta z}\\
&\left.\times\left(H_{2x;i,j,k}+H_{2y;i,j,k}+H_{2z;i,j,k}+M^0_{icell,jcell,kcell}\right)\right],
\end{aligned} \tag{A.7}$$

$$\begin{aligned}
C_{223;i,j,k} &= \frac{1}{\Delta x^2\Delta y\Delta z}\left[4\left(f_{i,j,k}+f_{iup,j,k}\right)+2\left(f_{i,jup,k}+f_{i,j,kup}+f_{iup,jup,k}+f_{iup,j,kup}\right)\right.\\
&+f_{i,jup,kup}+f_{iup,jup,kup}\\
&-\frac{2\mathrm{sgn}(\zeta_{i,j,k})}{\Delta x}\left\{4l_{x;icell,j,k}+2\left(l_{x;icell,jup,k}+l_{x;icell,j,kup}\right)+l_{x;icell,jup,kup}\right\}\\
&-\frac{3\mathrm{sgn}(\eta_{i,j,k})}{\Delta y}\left\{2\left(l_{y;i,jcell,k}+l_{y;iup,jcell,k}\right)+l_{y;i,jcell,kup}+l_{y;iup,jcell,kup}\right\}\\
&-\frac{3\mathrm{sgn}(\theta_{i,j,k})}{\Delta z}\left\{2\left(l_{z;i,j,kcell}+l_{z;iup,j,kcell}\right)+l_{z;i,jup,kcell}+l_{z;iup,jup,kcell}\right\}\\
&\left.+\frac{18\mathrm{sgn}(\zeta_{i,j,k})\mathrm{sgn}(\eta_{i,j,k})\mathrm{sgn}(\theta_{i,j,k})}{\Delta x\Delta y\Delta z}\right.
\end{aligned}$$

$$\times \left\{6H_{3x;i,j,k} + 2\left(H_{2y;i,j,k} + H_{2z;i,j,k}\right) + M^0_{icell,jcell,kcell}\right\}\Big], \tag{A.8}$$

$$\begin{aligned}
C_{233;i,j,k} &= \frac{-1}{\Delta x^2\Delta y^2\Delta z}\left[2\left(f_{i,j,k} + f_{iup,j,k} + f_{i,jup,k} + f_{iup,jup,k}\right)\right. \\
&+ f_{i,j,kup} + f_{i,jup,kup} + f_{iup,j,kup} + f_{iup,jup,kup} \\
&- \frac{2\mathrm{sgn}(\zeta_{i,j,k})}{\Delta x}\left\{2\left(l_{x;icell,j,k} + l_{x;icell,jup,k}\right) + l_{x;icell,j,kup} + l_{x;icell,jup,kup}\right\} \\
&- \frac{2\mathrm{sgn}(\eta_{i,j,k})}{\Delta y}\left\{2\left(l_{y;i,jcell,k} + l_{y;iup,jcell,k}\right) + l_{y;i,jcell,kup} + l_{y;iup,jcell,kup}\right\} \\
&- \frac{3\mathrm{sgn}(\theta_{i,j,k})}{\Delta z}\left\{l_{z;i,j,kcell} + l_{z;iup,j,kcell} + l_{z;i,jup,kcell} + l_{z;iup,jup,kcell}\right\} \\
&+ \frac{24\mathrm{sgn}(\zeta_{i,j,k})\mathrm{sgn}(\eta_{i,j,k})\mathrm{sgn}(\theta_{i,j,k})}{\Delta x\Delta y\Delta z} \\
&\left.\times\left\{3\left(H_{3x;i,j,k} + H_{3y;i,j,k}\right) + H_{2z;i,j,k}\right\}\right],
\end{aligned} \tag{A.9}$$

$$\begin{aligned}
C_{333;i,j,k} &= \frac{1}{\Delta x^2\Delta y^2\Delta z^2}\left[f_{i,j,k} + f_{iup,j,k} + f_{i,jup,k} + f_{i,j,kup}\right. \\
&+ f_{iup,jup,k} + f_{i,jup,kup} + f_{iup,j,kup} + f_{iup,jup,kup} \\
&- \frac{2\mathrm{sgn}(\zeta_{i,j,k})}{\Delta x}\left\{l_{x;icell,j,k} + l_{x;icell,jup,k} + l_{x;icell,j,kup} + l_{x;icell,jup,kup}\right\} \\
&- \frac{2\mathrm{sgn}(\eta_{i,j,k})}{\Delta y}\left\{l_{y;i,jcell,k} + l_{y;i,jcell,kup} + l_{y;iup,jcell,k} + l_{y;iup,jcell,kup}\right\} \\
&- \frac{2\mathrm{sgn}(\theta_{i,j,k})}{\Delta z}\left\{l_{z;i,j,kcell} + l_{z;iup,j,kcell} + l_{z;i,jup,kcell} + l_{z;iup,jup,kcell}\right\} \\
&+ \frac{8\mathrm{sgn}(\zeta_{i,j,k})\mathrm{sgn}(\eta_{i,j,k})\mathrm{sgn}(\theta_{i,j,k})}{\Delta x\Delta y\Delta z} \\
&\left.\times\left\{6\left(H_{3x;i,j,k} + H_{3y;i,j,k} + H_{3z;i,j,k}\right) - M^0_{icell,jcell,kcell}\right\}\right],
\end{aligned} \tag{A.10}$$

where $\Delta x = x_{iup} - x_i$, $\Delta y = y_{jup} - y_j$, $\Delta z = z_{kup} - z_k$, and,

$$\begin{aligned}
H_{1z;i,j,k} &= H_1\left(z_k, \Delta z, M^m_{z;icell,jcell,kcell}\right) \\
&= \frac{1}{\Delta z^2}\left[\left(10z_k^2 + 12z_k\Delta z + 3\Delta z^2\right)M^0_{icell,jcell,kcell}\right. \\
&\left.-4\left\{\left(5z_k + 3\Delta z\right)M^1_{z;icell,jcell,kcell} - 5M^2_{z;icell,jcell,kcell}\right\}\right],
\end{aligned} \tag{A.11}$$

$$\begin{aligned}
H_{2z;i,j,k} &= \frac{1}{\Delta z^2}\left[\left(15z_k^2 + 16z_k\Delta z + 3\Delta z^2\right)M^0_{icell,jcell,kcell}\right. \\
&\left.-2\left\{\left(15z_k + 8\Delta z\right)M^1_{z;icell,jcell,kcell} - 15M^2_{z;icell,jcell,kcell}\right\}\right],
\end{aligned} \tag{A.12}$$

$$\begin{aligned}
H_{3z;i,j,k} &= \frac{1}{\Delta z^2}\left[\left(5z_k^2 + 5z_k\Delta z + \Delta z^2\right)M^0_{icell,jcell,kcell}\right. \\
&\left.-5\left\{\left(2z_k + \Delta z\right)M^1_{z;icell,jcell,kcell} - 2M^2_{z;icell,jcell,kcell}\right\}\right].
\end{aligned} \tag{A.13}$$

Remaining coefficients can be obtained on the basis of a cyclic rule. For example, replacing $(x, y, z) \to (z, x, y)$, $(\zeta, \eta, \theta) \to (\theta, \zeta, \eta)$, and $(i, j, k) \to$

(k, i, j) in Equation (A.5) (e.g., $l_{x;icell,jup,k} \rightarrow l_{z;iup,j,kcell}$) gives $C_{312;i,j,k}$.

References

Birdsall, C. K., Langdon, A. B., 1991. Plasma Physics via Computer Simulation. Inst. of Phys. Publishing, Bristol/Philadelphia.

Cheng, C. Z., Knorr, G., Nov. 1976. The integration of the Vlasov equation in configuration space. Journal of Computational Physics 22, 330–351.

Crouseilles, N., Respaud, T., Sonnendrücker, E., Oct. 2009. A forward semi-Lagrangian method for the numerical solution of the Vlasov equation. Computer Physics Communications 180, 1730–1745.

Filbet, F., Sonnendrücker, E., Bertrand, P., Sep. 2001. Conservative Numerical Schemes for the Vlasov Equation. Journal of Computational Physics 172, 166–187.

Gottlieb, S., Shu, C. W., Jan. 1998. Total variation diminishing Runge-Kutta schemes. Mathematics of Computation 67, 73–85.

Gurnett, D. A., Bhattacharjee, A., Jan. 2005. Introduction to Plasma Physics. Cambridge University Press.

Hoshino, M., 1986. Theoretical and Computational Studies of Plasma Kinetic Phenomena: Tearing Mode Instability and Foreshock Cyclotron Interaction. Ph.D. thesis, Univ. Tokyo.

Hoshino, M., Jul. 1987. The electrostatic effect for the collisionless tearing mode. Journal of Geophysical Research 92, 7368–7380.

Ii, S., Xiao, F., Mar. 2007. CIP/multi-moment finite volume method for Euler equations: A semi-Lagrangian characteristic formulation. Journal of Computational Physics 222, 849–871.

Jiang, G., Shu, C., Jun. 1996. Efficient Implementation of Weighted ENO Schemes. Journal of Computational Physics 126, 202–228.

Mangeney, A., Califano, F., Cavazzoni, C., Travnicek, P., Jul. 2002. A Numerical Scheme for the Integration of the Vlasov-Maxwell System of Equations. Journal of Computational Physics 179, 495–538.

Minoshima, T., Matsumoto, Y., Amano, T., Jul. 2011. Multi-moment advection scheme for Vlasov simulations. Journal of Computational Physics 230, 6800–6823.

Nakamura, T., Yabe, T., Aug. 1999. Cubic interpolated propagation scheme for solving the hyper-dimensional Vlasov-Poisson equation in phase space. Computer Physics Communications 120, 122–154.

Shu, C., Osher, S., Aug. 1988. Efficient Implementation of Essentially Non-oscillatory Shock-Capturing Schemes. Journal of Computational Physics 77, 439–+.

Sydora, R. D., Sauer, K., Silin, I., Nov. 2007. Coherent whistler waves and oscilliton formation: Kinetic simulations. Geophysical Research Letters 342, L22105.

Takizawa, K., Yabe, T., Nakamura, T., Oct. 2002. Multi-dimensional semi-Lagrangian scheme that guarantees exact conservation. Computer Physics Communications 148, 137–159.

Yabe, T., Tanaka, R., Nakamura, T., Xiao, F., Feb. 2001. An Exactly Conservative Semi-Lagrangian Scheme (CIP-CSL) in One Dimension. Mon. Wea. Rev. 129, 332–344.

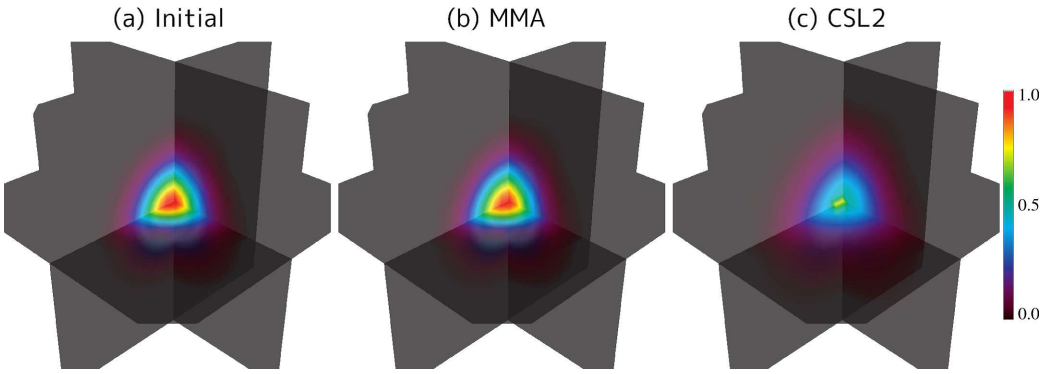

Figure 1: Three-dimensional solid body rotation problem of a symmetric gaussian profile. (a) Initial profile. (b,c) Profiles after 100 rotations calculated with the MMA and CIP-CSL2 schemes.

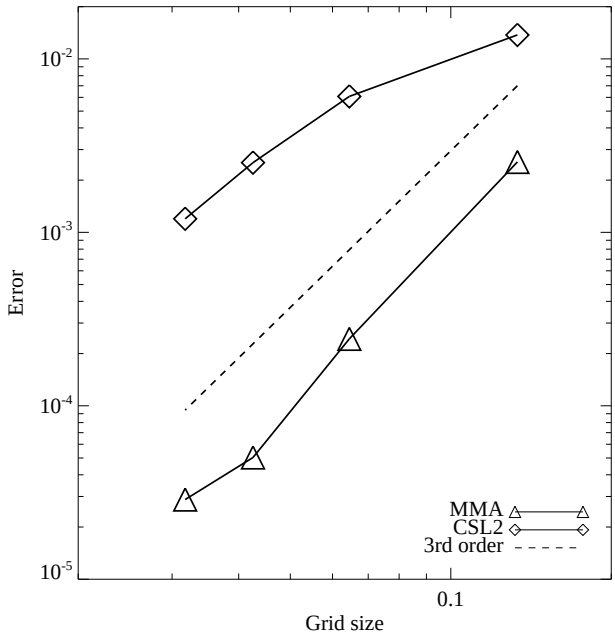

Figure 2: Errors of the three-dimensional solid body rotation problem of a symmetric gaussian profile as a function of the grid size. Triangles and diamonds are obtained from the MMA and CIP-CSL2 schemes. A dashed line indicates the third order accuracy.

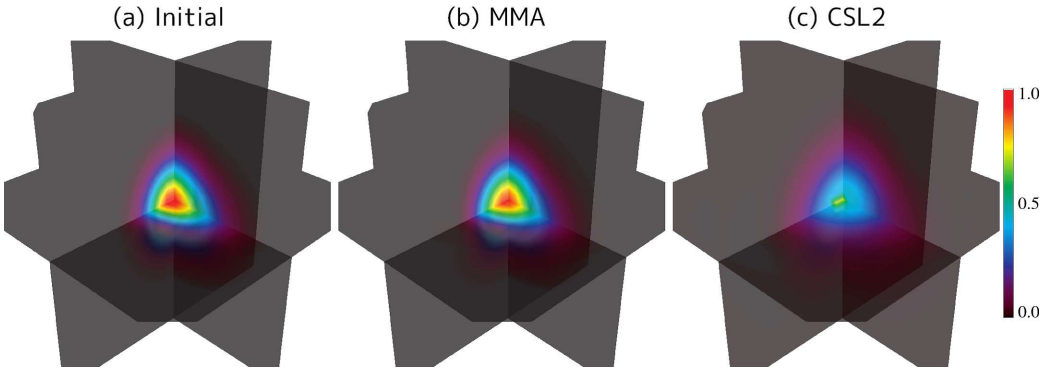

Figure 3: Three-dimensional solid body rotation problem of an asymmetric gaussian profile. The format is same as Fig. 1.

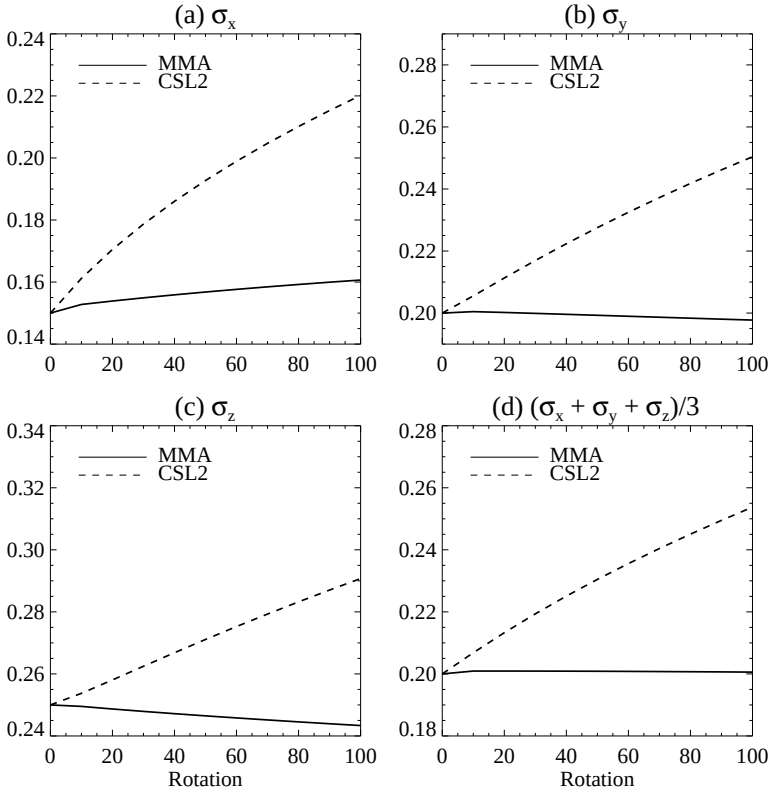

Figure 4: Temporal variation of the standard deviation (a) σ_x, (b) σ_y, (c) σ_z, and (d) their average in the three-dimensional solid body rotation problem of an asymmetric gaussian profile. Solid and dashed lines are obtained from the MMA and CIP-CSL2 schemes.

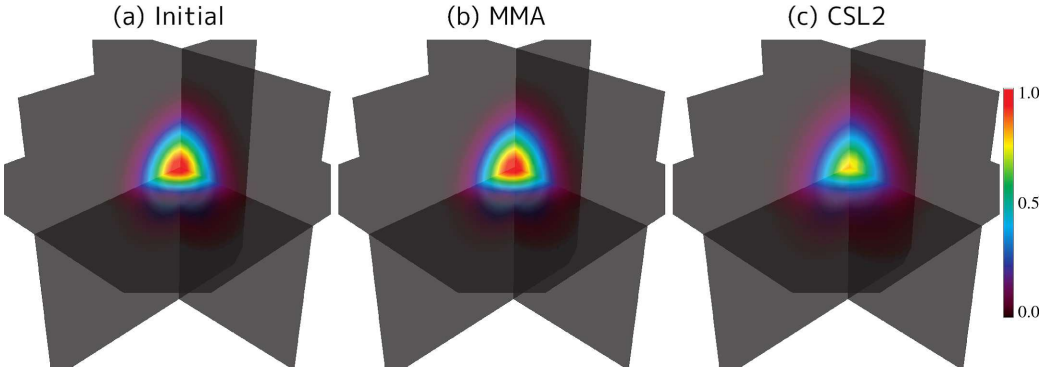

Figure 5: Three-dimensional solid body rotation and advection problem of a symmetric gaussian profile. The format is same as Fig. 1.

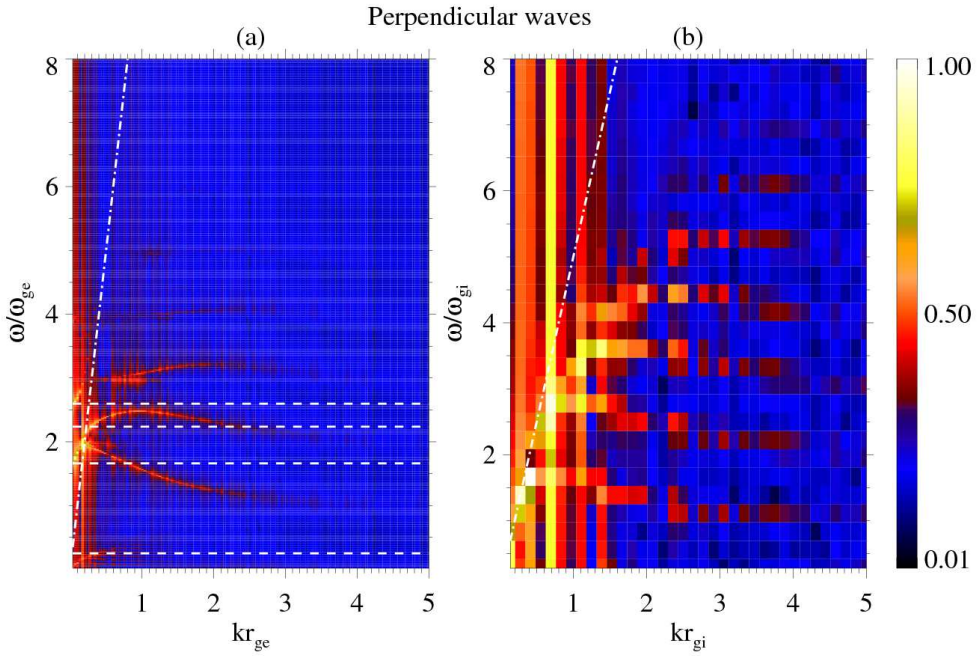

Figure 6: Electromagnetic Vlasov simulation of perpendicular-propagating waves. Color contour shows the Fourier amplitude of the electrostatic field E_x (normalized by its maximum value). (a) The simulation result until $\omega_{pe}t = 361.3$. Horizontal and vertical axes are the wavenumber and frequency normalized by the inverse electron gyro radius and the electron gyro frequency. The amplitude is exponentiated by 0.15 for illustration. From top to bottom, dashed lines represent the R-mode cutoff, upper hybrid, L-mode cutoff, and lower hybrid frequencies. A dot-dashed line represents the dispersion relation of the light mode in vacuum. (b) The simulation result until $\omega_{pe}t = 723.4$. Horizontal and vertical axes are the wavenumber and frequency normalized by the inverse proton gyro radius and the proton gyro frequency. The amplitude is exponentiated by 0.3. A dot-dashed line represents the dispersion relation of the Alfvén wave.

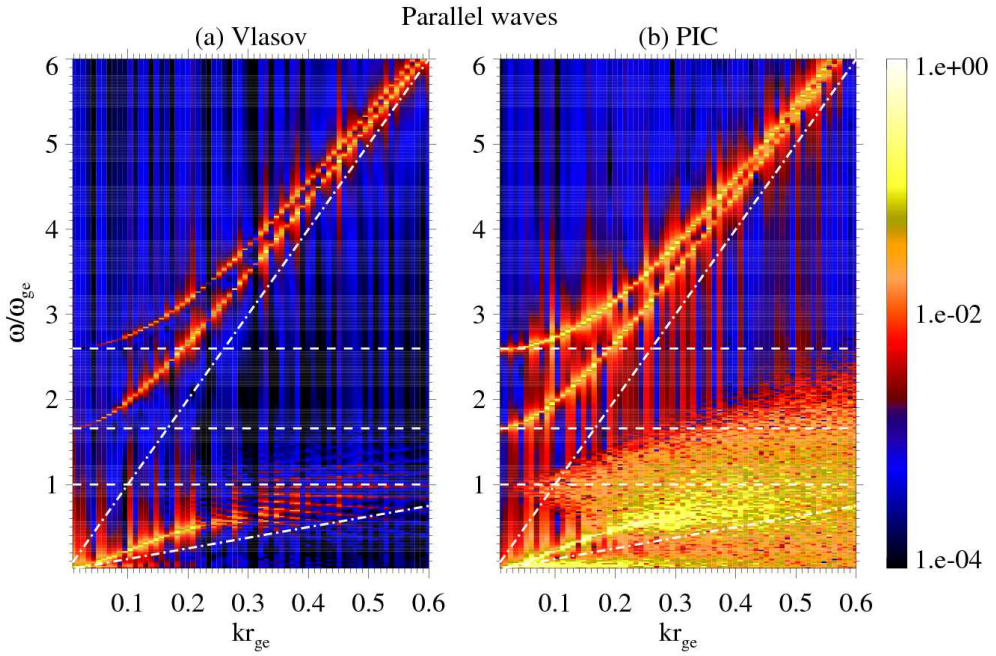

Figure 7: Electromagnetic (a) Vlasov and (b) PIC simulations of parallel-propagating waves. Color contour shows the Fourier amplitude of the transverse field B_y (normalized by its maximum value). Horizontal and vertical axes are the wavenumber and frequency normalized by the inverse electron gyro radius and the electron gyro frequency. From top to bottom, dashed lines represent the R-mode cutoff, L-mode cutoff, and electron gyro frequencies. Dot-dashed lines represent the dispersion relation of the light mode in vacuum and the Alfvén wave.

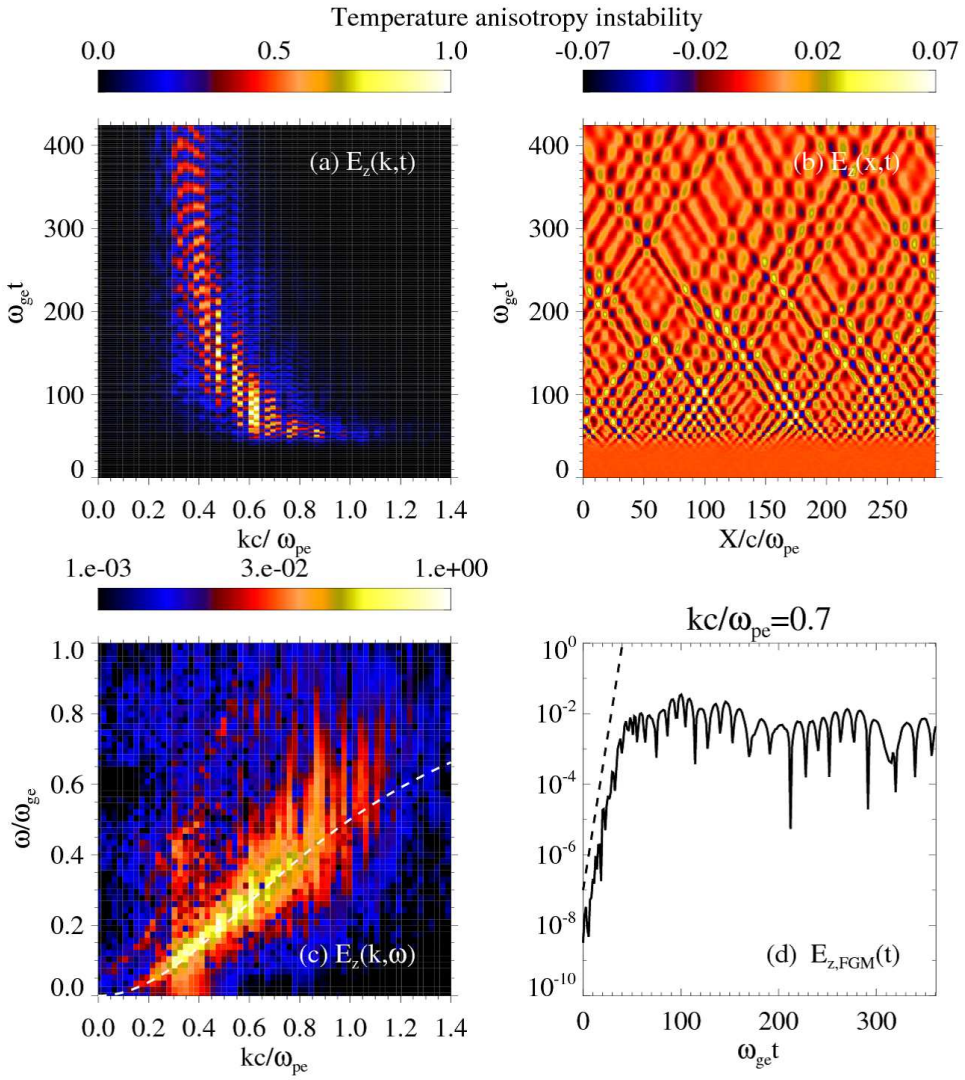

Figure 8: Electromagnetic Vlasov simulation of the electron temperature anisotropy instability. (a,b) Time profile of the transverse electric field spectrum $E_z(k,t)$ (normalized by its maximum value) and distribution $E_z(x,t)$. (c) Fourier spectrum of the transverse electric field $E_z(k,\omega)$ (normalized by its maximum value). A dashed line represents the linear dispersion relation of the whistler wave. (d) Time profile of E_z at the wavenumber corresponding to the fastest growing mode ($kc/\omega_{pe} = 0.7$). A dashed line indicates the linear growth rate.

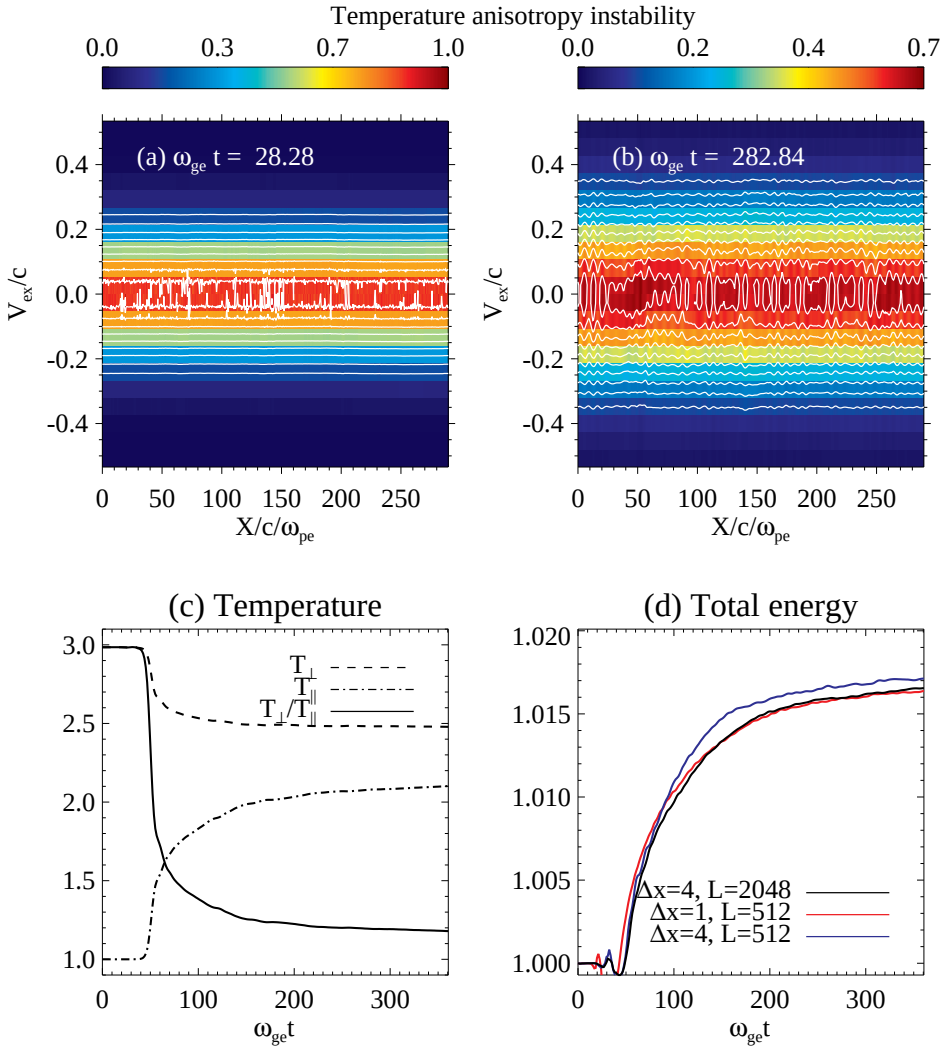

Figure 9: Electromagnetic Vlasov simulation of the electron temperature anisotropy instability. (a,b) Longitudinal electron distribution function at linear ($\omega_{ge}t = 28.3$) and nonlinear ($\omega_{ge}t = 283$) phases. (c) Time profile of the perpendicular temperature (dashed line), parallel temperature (dot-dashed line), and temperature anisotropy (solid line). The temperatures are normalized by the initial value of the parallel temperature. (d) Time profile of the total energy (normalized by its initial value). Black, red, and blue lines are obtained from different simulation runs with $(\Delta x/\lambda_D, L/\lambda_D) = (4, 2048), (1, 512),$ and $(4, 512)$, respectively.